Islamic Azad University

Journal of
Optoelectronical Nanostructures

Autumn 2020 / Vol. 5, No. 4

Electronic and Optical Properties of SnGe and SnC Nanoribbons: A First-Principles Study

Samira Damizadeh[1], Maryam Nayeri*[,1], Forough Kalantari Fotooh[2], Somayeh Fotoohi[3]

[1] Department of Electrical Engineering, Yazd Branch, Islamic Azad University, Yazd, Iran.

[2]Department of Chemistry, Yazd Branch, Islamic Azad University, Yazd, Iran

[3]Department of Electrical Engineering, Islamshahr Branch, Islamic Azad University, Islamshahr, Iran

(Received 24 Sep. 2020; Revised 28 Oct. 2020; Accepted 24 Nov. 2020; Published 15 Dec. 2020)

Abstract: Structural, electronic, and optical properties of one-dimensional (1D) SnGe and SnC with two types (armchair and zigzag) and different widths are studied by using first-principles calculations. The atoms of these structures in edges are passivated by hydrogen. The results show armchair SnGe and SnC nanoribbons (A-SnXNRs, X=Ge, C) are the direct semiconducting and divided into three distinct families W=3p, W=3p+1, and W=3p+2, (p is a positive integer). By increasing width, the band gaps converge to 1.71 eV and 0.15 eV for A-SnCNRs and A-SnGeNRs, respectively. Furthermore, the position of the first peak of the dielectric function in both of them occurs in their value of direct band gap at Γ point. also, the absorption coefficient for 9, 11, 13 A-SnCNRs displays that there is no absorption at the lower energy range from 0 to 1.2 eV, whereas absorption characteristics for 9, 11, and 13 A-SnGeNRs appeared at near-infrared to the visible spectrum. These results can provide important information for the use of Group IV binary compounds in electronic devices.

Keywords: SnC and SnGe Nanoribbon, Electronic Properties, Dielectric Function, First-Principles Study.

1. INTRODUCTION

The nanomaterials such as carbon nanotube, graphdiyne, graphene, and quantum-dot cellular automata (QCA) have been the topic of several experimental and theoretical investigations because of their exceptional charge transport and broad applications in many emerging areas [1-5]. However, the zero

---

* Corresponding author. Email: **nayeri@iauyazd.ac.ir**

bandgap of graphene possesses an inherent problem in optoelectronic applications [6-8]. Thus, nowadays, many researchers have focused on graphene-like two-dimensional (2D) materials with a finite band gap such as XC (X=Si, Ge, Sn), SnX (X=Si, Ge) nanosheet [9, 10].

According to experimental research, nanostructures of SiC and GeC, and ultrathin 2D-SiC film have been prepared through solution-based exfoliation [10].

Ball milling technique has been widely applied to achieve nanocrystalline solids, various alloys, and composites with equilibrium structure at room temperature [11]. Using X-ray Absorption Fine Structure Spectroscopy (XAFS), the researchers have shown that ball milling of Sn/Ge and Sn/Si powders fabricates surface layers of SnGe and SnSi alloys around Ge and Si particles [9].

Several authors have investigated the electronic and optical properties of these binary compounds [12- 18]. Previous theoretical studies have shown that SiC, GeC, and SnC nanosheets have 2D flat honeycomb structures that are related to strong bonding between two nearest-neighbor Pz orbitals [14] while the SiGe, SnSi and SnGe sheets have Puckered structures similar to silicene and germanene [16].

Şahin et al. have studied optimized structures, cohesive energies, electronic band structures of group-IV elements (graphene, Si, Ge), and their binary compounds (SiC, GeC, SnGe, SiGe, SnSi, SnC). Their results demonstrated that the binary compounds of group-IV are direct or indirect semiconductors and the values of band gap depend on the constituent atoms.

Tremendous efforts have been attempted to indirect–direct band gap transition in SnC nanosheet to make it appropriate for optoelectronic devices.

Lu et al. have investigated the electronic properties of graphene, SiC, GeC, and SnC monolayers under different strained conditions using density functional theory DFT and the quasi-particle GW approximation. They exhibit that SnC nanosheet has an indirect gap of 1.71 eV along the Γ-K direction. The calculated band structure shows that indirect–direct band gap transition is observed for the group-IV carbides by strain engineering [20].

Majidi et al. have reported the impact of various point defects on the atomic structures and the electronic properties of SnC sheet by employing the first-principles calculations. Their results show that the SnC sheet including Stone–Wales (SW) defect preserves semiconductor behavior with the direct band gap of 0.54 eV [21].

Jin et al have reported the structural and electronic properties of SiC, GeC, and SnC by surface chemical modifications, i.e. hydrogenation, halogenation, and hydroxylation. Their results show that the indirect-direct band gap transition of SiC, SnC can be observed through adatom decoration [22].

One of the explored strategies to tune the band gap of nanosheets is forming nanoribbons [23].

In our previous research, we investigated the electronic structure and optical of armchair SnSi nanoribbons (A-SnSiNR) with different widths based on density functional theory DFT. We found that there are three distinct families of A-SnSiNR as 3p - 1, 3p, and 3p + 1 (where p is an integer). Furthermore, all A-SnSiNR families have semiconductor behavior. The band gap energy for the case of 3p + 1 is greater than the other two groups [12].

In the present work, we pattern SnX (X= C, Ge) nanosheet into a nanoribbon (NR) in which the carriers are confined to a quasi-one-dimensional (1D) system. In the NR structures, all the dangling bonds at the edge of the NRs are passivated with one hydrogen atom. According to their edge shape, SnXNRs have two typical types; i.e., Armchair-SnXNRs (A-SnXNRs) and Zigzag-SnXNRs (Z-SnXNRs). We consider different widths of A-SnXNRs and Z-SnXNRs and study their electronic and optical properties by performing first-principle calculations.

This paper is given the following structure: In Section 2, computation methods are illustrated. The electronic and optical properties of A-SnXNRs and Z-SnXNRs are presented in Section 3. Finally, the conclusions are explained in section 4.

2. COMPUTATIONAL METHODS

In this work, we investigate the electronic and optical properties of W A-SnXNRs and W Z-SnXNRs (X= C, Ge) with different widths, where W is the number of dimmer lines across the ribbon width. Their electronic and optical properties are calculated by the first-principles method within the framework of DFT. All DFT calculations are performed using the Vienna Ab initio simulation package (VASP) [24]. The norm-conserving Troullier–Martins pseudopotential is used to describe the interaction between valence electrons and the atomic core [25]. The electronic exchange-correlation energy was determined using the generalized gradient approximation (GGA) in the parametrization by Perdew, Burke, and Ernzerhof [26]. To simulate an NR, the periodic boundary condition (PBC) is considered along its length (z-direction). Furthermore, a vacuum space of 20 Å is taken along two other directions to isolate the neighboring NRs in x- and y-direction, respectively.

As a typical example, the top and side view of orthorhombic supercells of 10 Z-SnXNR and 11A-SnXNR are shown in figure 1. The edge atoms of the 11 A-SnXNR and 11 Z-SnXNR are saturated with H-atoms. The directions of x, y, and z are shown in figure 1.

Self-consistent calculations are performed with an iteration control parameter tolerance lower than 0.0001. The k-point sampling is 1×10×10 in the x, y, and z-direction, and the mesh cutoff is set to 150 Rydberg. All SnXNRs were fully relaxed until all residual forces on each atom are less than 0.05 eV/Å.

In general, the optical response of solids to the electromagnetic field is directly connected to the complex dielectric function ε(ω) [27]:

$$\varepsilon(\omega) = \varepsilon_1(\omega) + i\varepsilon_2(\omega) \tag{1}$$

Here, $\varepsilon_1(\omega)$ and $\varepsilon_2(\omega)$ are the real and imaginary part of the dielectric function.

The calculations of an imaginary part are described using time dependent perturbation theory (TDPT) with dipole approximation.

The imaginary part $\varepsilon_2(\omega)$ of the dielectric function is calculated by summing all the direct interband transitions from the occupied to unoccupied states over the Brillouin zone, which are the direct output of band structure calculation. also, $\varepsilon_2(\omega)$ is obtained using the following expression [27].

$$\varepsilon_2(\omega) = \frac{4\pi^2}{m^2\omega^2} \cdot \sum_{V\cdot C} \int_{BZ} d^3 k \frac{2}{2\pi} |e \cdot M_{CV}(K)|^2 \times [E_C(K) - E_V(K) - \hbar\omega] \tag{2}$$

Where *e* is the electric quantity of electrons and ω shows the frequency of the electromagnetic radiation, respectively. The indices c and v represent the conduction band and the valence band, respectively. In addition, *K* is a reciprocal lattice vector and $|e.M_{CV}(K)|$ is the momentum matrix element.

The real part of the dielectric function $\varepsilon_1(\omega)$ is obtained using the usual Kramers- Kronig transformation [27]:

$$\varepsilon_1(\omega) = 1 + \frac{8\pi e^2}{m^2} \cdot \sum_{V\cdot C} \int_{BZ} d^3 k \frac{2}{2\pi} \frac{|e\cdot M_{CV}(K)|^2}{[E_C(K)-E_V(K)]} \times \frac{\hbar^3}{[E_C(K)-E_V(K)]^2-\hbar^2\omega^2} \tag{3}$$

The absorption coefficient can also be evaluated using the formula

$$\alpha(E) = \frac{2E(eV)}{\hbar c} \sqrt{\frac{\sqrt{\varepsilon_1{}^2(\omega)+\varepsilon_2{}^2(\omega)}-\varepsilon_1(\omega)}{2}} \tag{4}$$

Where c, α, and h represent the speed of light in vacuum, absorption coefficient, and Planck contact, respectively, and ħ = h/2π.

3. RESULTS AND DISCUSSION

Figure 1(a)-(b) show top and side view 10 Z-SnCNR and 11 A-SnCNR supercells, as well as figure 1(c)-(d) present top and side view 10 Z-SnGeNR and 11 A-SnGeNR supercells with W=11 after full geometry optimization. As shown in these figures, the geometric structures of SnCNRs are a planner. However, the atoms of SnGeNRs are out of plane about 0.73 Å and they have puckered structures. Sn, C, and Ge atoms contribute their valance electrons $4d^{10}$ $5s^2$ $5p^2$, $2s^2$ $2p^2$, and $3d^{10}$ $4s^2$ $4p^2$ respectively.

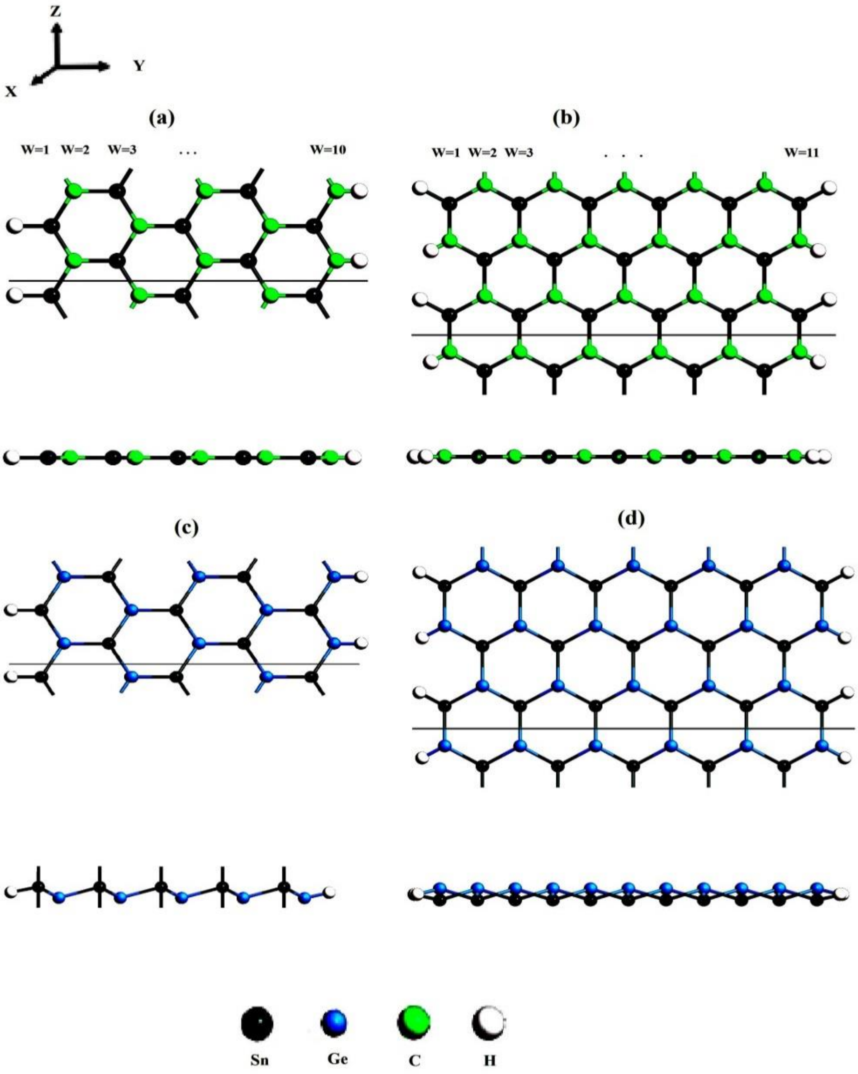

Fig.1 Top and side view of optimized structures for (a) 10 Z-SnCNR, (b) 11 A-SnCNR (c) 10 Z-SnGeNR, and (d) 11 A-SnGeNR.

The calculated lattice constant of our structures, bonds' lengths between the neighboring atoms in SnCNRs and SnGeNRs are presented for the relaxed structures in Table 1.

TABLE 1

The calculated of a lattice constant, average bond length, and thickness of sheet for A-SnXNR and Z-SnXNR.

Structure		A-SnCNR	Z-SnCNR
Lattice Constant (Å)		3.55	3.55
Bond Length (Å)	Sn-C	2.05	2.05
	Sn-H	1.73	1.73
	C-H	1.09	1.09
Thickness of sheet (Å)		0	0

Structure		A-SnGeNR	Z-SnGeNR
Lattice Constant (Å)		4.27	4.27
Bond Length (Å)	Sn-Ge	2.57	2.57
	Sn-H	1.76	1.76
	Ge-H	1.58	1.58
Thickness of sheet (Å)		0.73	0.73

The band structures of W Z-SnCNRs and W Z-SnGeNRs (W= 16, 18, and 20) are presented in figures 2 and 3, respectively.

In the case of W Z-SnGeNRs, the results exhibit valence and conduction bands touch the Fermi level at the Γ point and show metallic behavior (zero band gap) whereas W Z-SnCNRs have very small band gap energy.

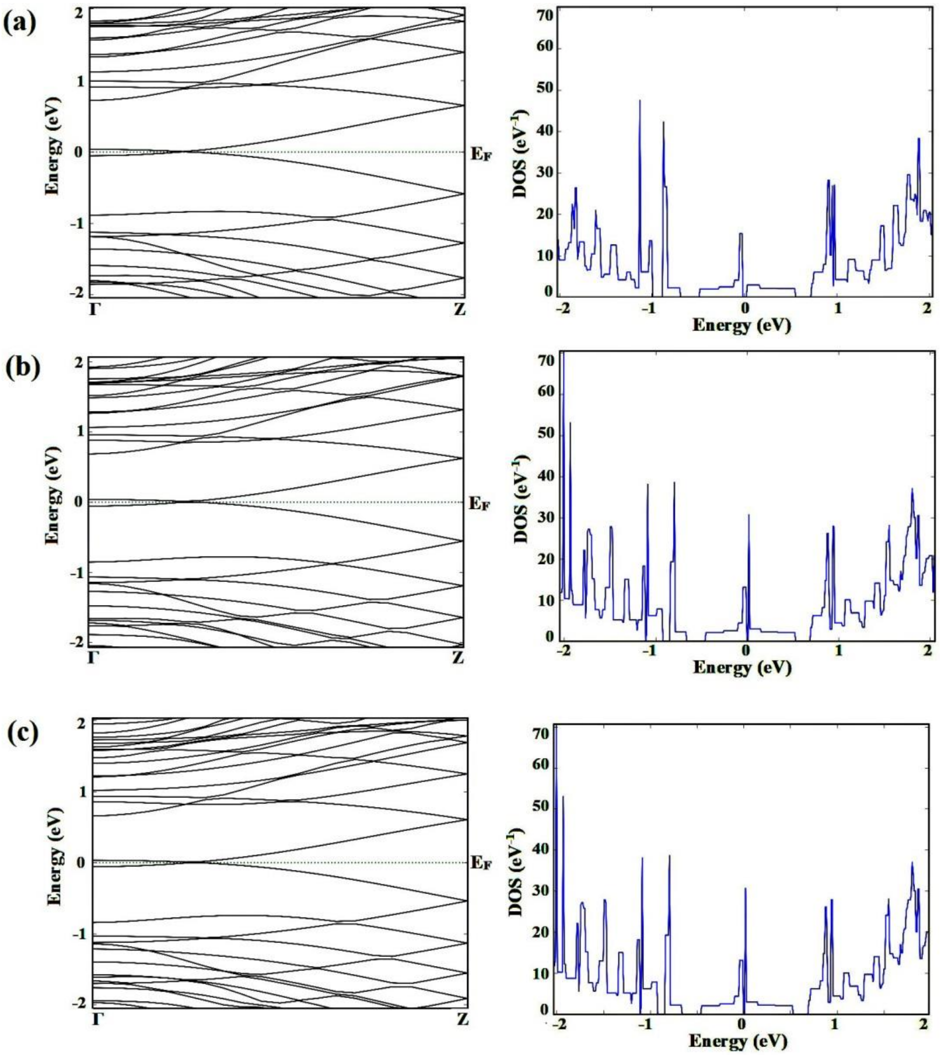

Fig. 2 The electronic band structures and DOS for W Z-SnCNRs with the width of (a) W=16, (b) W=18, and (c) W=20.

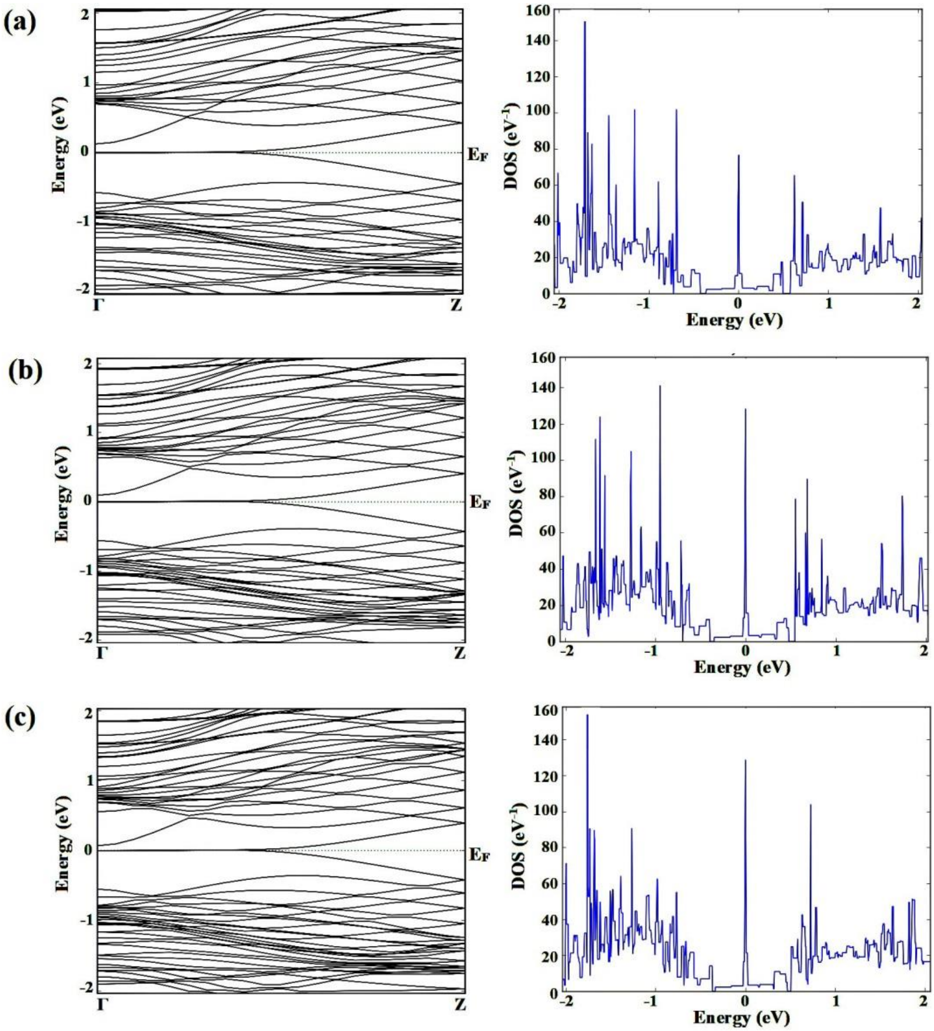

Fig. 3 The electronic band structures and DOS for W Z-SnGeNRs with the width of (a) W=16, (b) W=18, and (c) W=20.

The band structures and DOS for A-SnXNRs with widths include W=9, 11, and 13 are shown in figures 4 to 5. It is observed that A-SnCNRs with the width of W=9, 11, and 13 have a finite direct band gap (in comparison to the indirect bandgap of SnC sheet) which the valance band maximum (VBM) and conduction band minimum (CBM) locates at Γ point. The computed band gap value for A-SnCNRs with the width of W=9, 11, and 13 are 1.70, 1.58, and 1.69 eV, respectively. This result guarantees the potential of A-SnCNRs for optoelectronics devices.

Furthermore, A-SnGeNRs with widths of W=9, 11, and 13 are semiconducting with a direct band gap of 0.31, 0.14, and 0.26 eV at the Γ point, respectively, as shown in figure 5.

As well as, the density of state (DOS) is shown for these structures. Their DOS is greatly consistent with their band structure in all assumed structures.

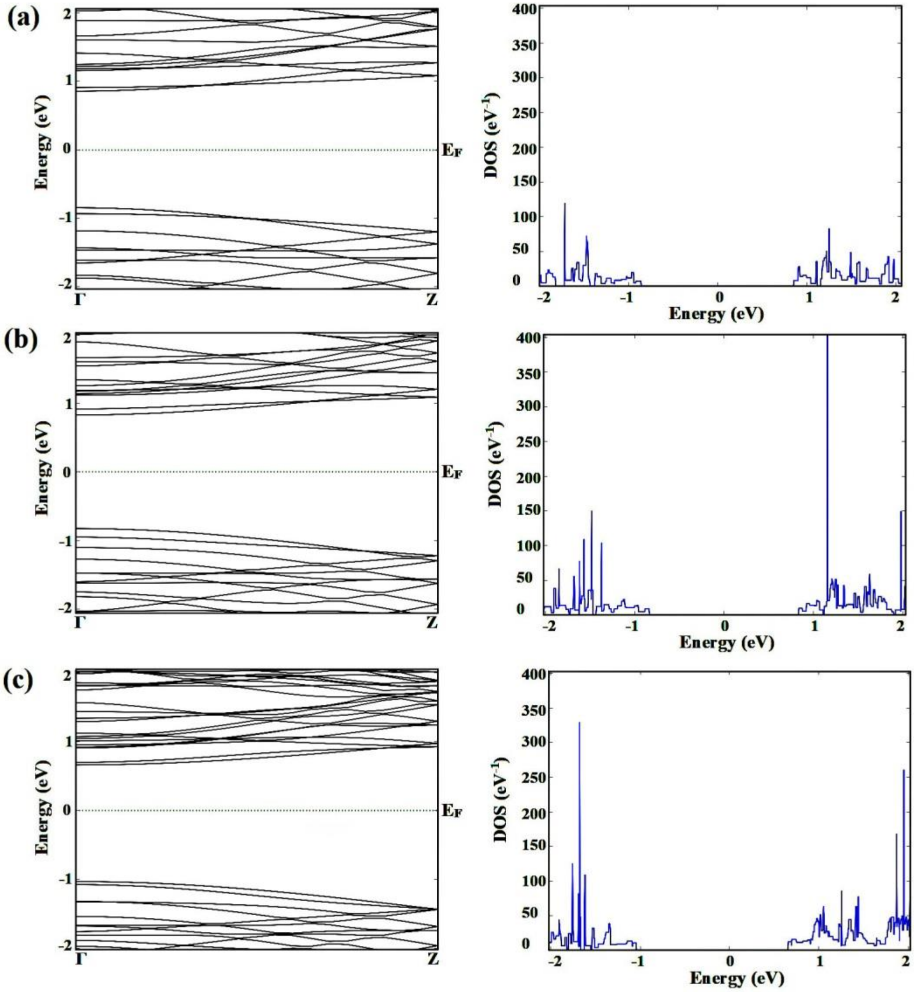

Fig. 4 The electronic band structures and DOS for W A-SnCNRs with the width of (a) W=9, (b) W=11, and (c) W=13.

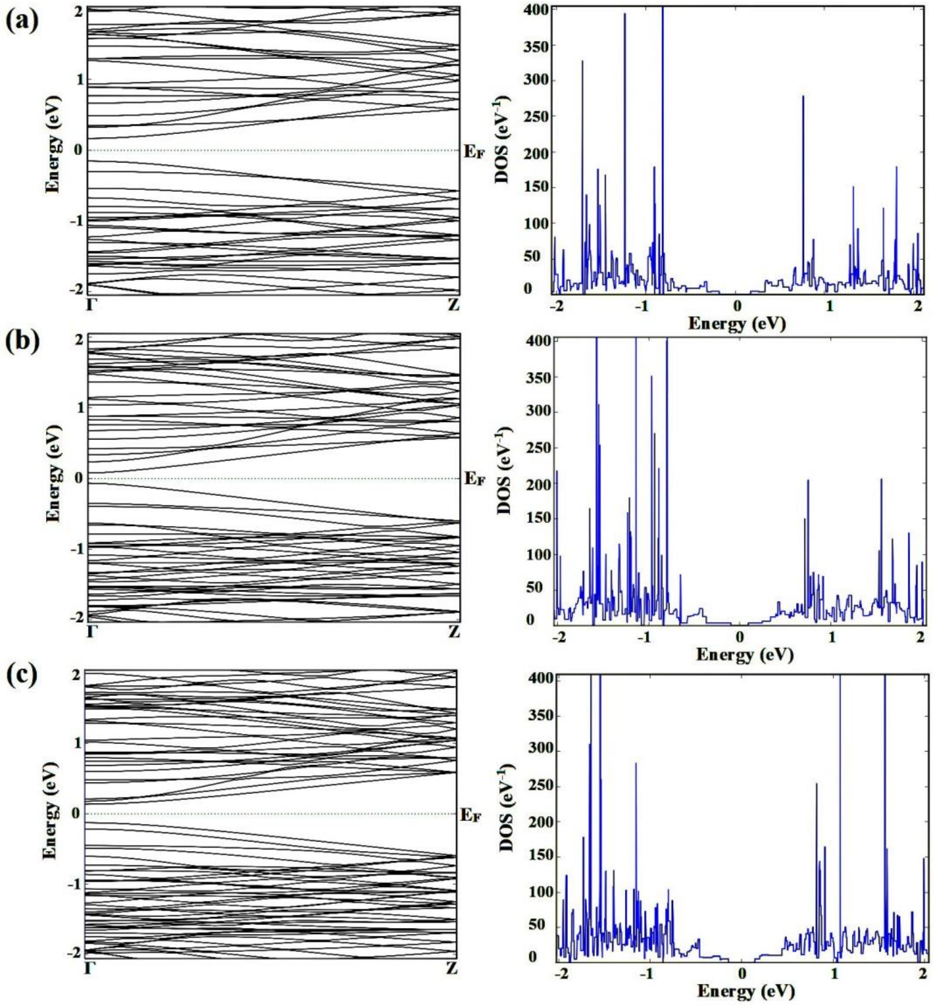

Fig. 5 The electronic band structures and DOS for W A-SnGeNRs with the width of (a) W=9, (b) W=11, and (c) W=13.

To explore the geometry dependency of the energy gap, we calculated the band gap of W A-SnXNRs with a width of W=5 to 21. The band gaps of W A-SnXNRs as a function of width are given in figure 6(a)-(b). As shown in these figures, all W A-SnXNRs are semiconducting and the band gap is dependent on the nanoribbon width. Depending on the W value, A-SNXNRs are separated into three different groups W=3p, W=3p+1, and W=3p+2, where p is a positive integer.

In the case of W A-SnCNRs, as the width increases, the band gap achieves a constant value of 1.71eV which is almost the band gap of SnC monolayer [15]. Also, the value of the band gap for the family N=3p is more than the band gap of N=3p+1 and 3p+2 families.

In the case of W A-SnGeNRs, the N=3p+1 family has much lower band gaps compared to the W A-SnGeNRs from N=3p and 3p+2 families. In addition, as the width increases, the band gaps finally converge to a constant value of 0.15 eV.

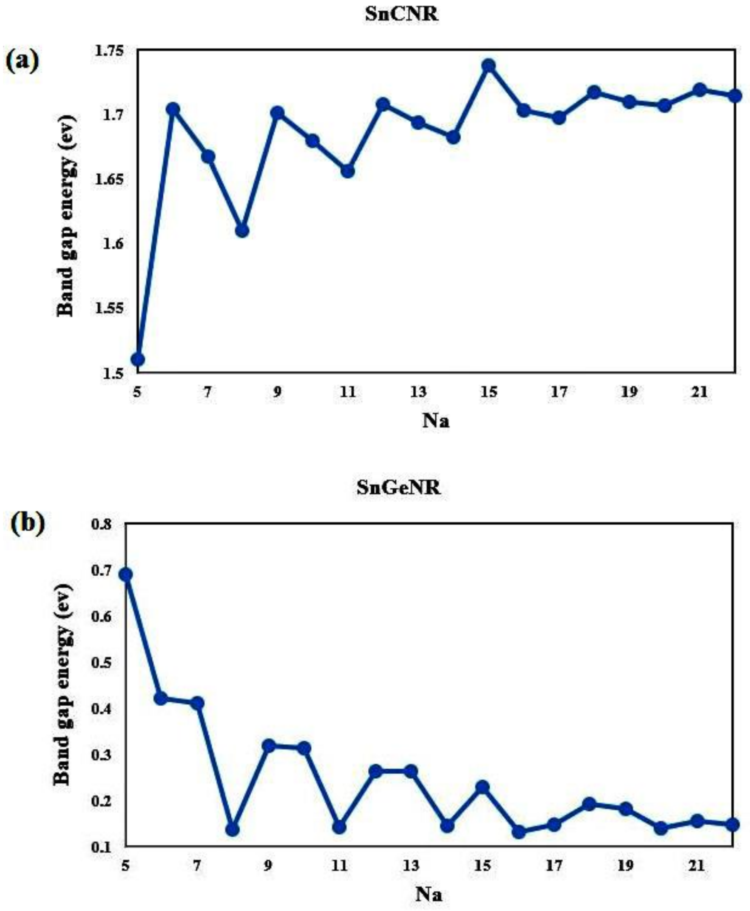

Fig. 6 Variation of band gaps of W A-SnXNRs as a function of Na (the number of atoms at the edge: 5 to 21) (a) W A-SnCNRs and (b) W A-SnCNRs.

In order to explain the states in detail, we calculated PDOS for the A-SnCNRs and A-SnGeNRs. We considered their valance electrons from these structures. PDOS is represented for A-SnCNRs and A-SnGeNRs with 11 atoms at the edge (W = 11) in figures 7 and 8, respectively.

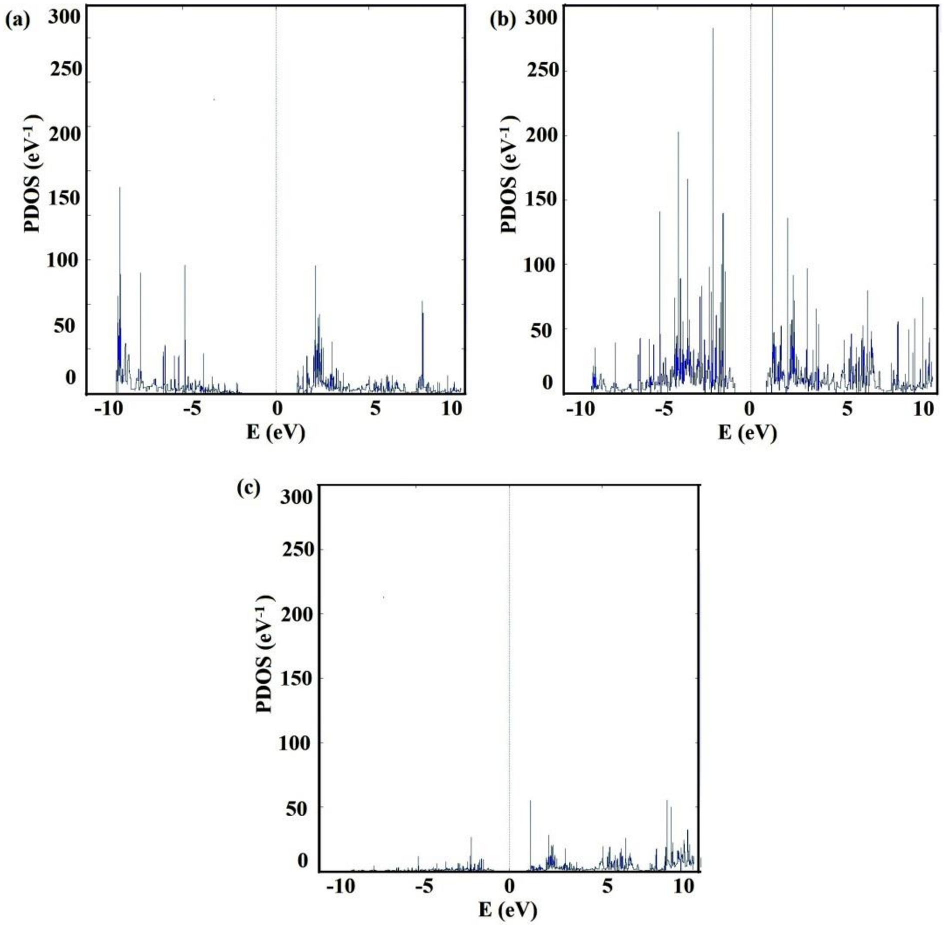

Fig. 7 The PDOS for A-SnCNRs with the width=11 and orbital of (a) s, (b) p, and (c) d.

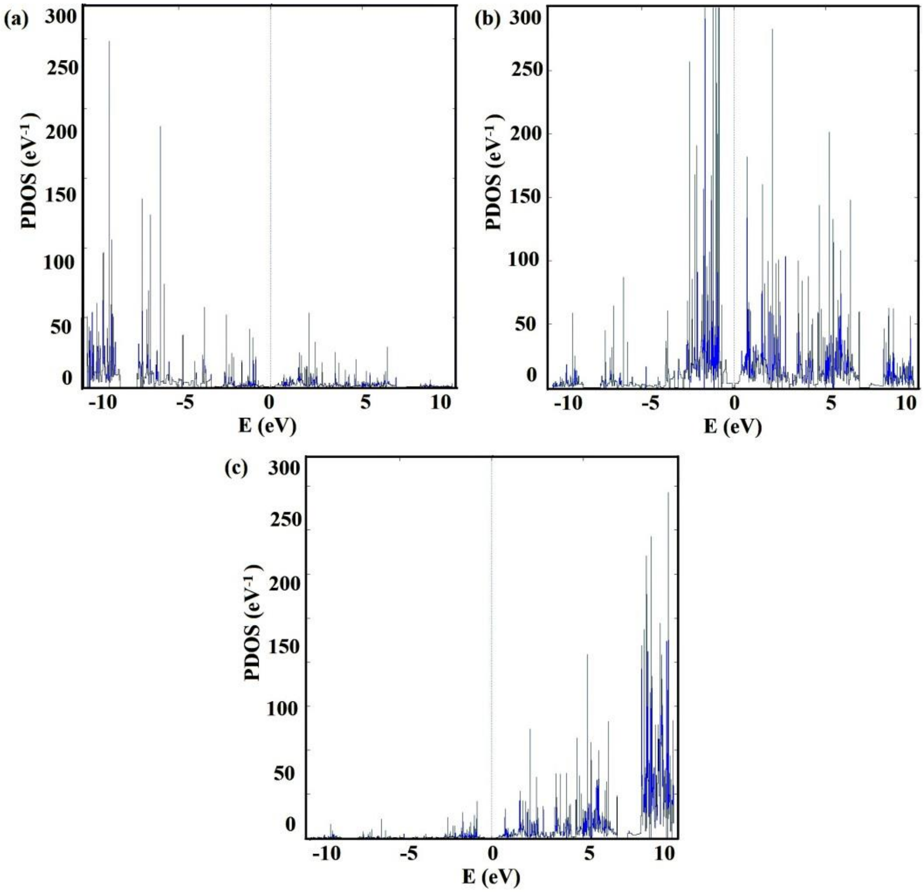

Fig. 8 The PDOS for A-SnGeNRs with W=11. (a) s, (b) p, and (c) d orbitals.

As seen from figures 7 and 8, compared to DOS, p orbitals of the valence electrons of these structures are effective near the Fermi level, while the s and d-orbitals are more effective at higher energies.

To investigate the effect of variation of widths in W A-SnXNRs (W=9, 11, 13), the real (lower panel) and imaginary parts (upper panel) of dielectric function are presented in figures 9 to 10. The real and imaginary parts of dielectric function determine the crystal response to the electromagnetic field which is the direct output of band structure calculation of a material. In our simulation, all the optical properties are computed in the photon energy range of 0 to 5 eV, which presents the relevant information in the ultraviolet, visible, and infrared regions of the electromagnetic spectra.

As shown in figure 9(a)-(c), the imaginary part of the dielectric function for the A-SnCNRs contains principal peaks that indicating the interband transition between the valence bands and the conduction bands. The first peak for 9, 11, and 13 A-SnCNRs locates at 1.85, 1.9, and 1.8 eV. As well as, the first peak for 9, 11, and 13 A-SnGeNRs occurs at 0.35, 0.2, and 0.3 eV (figure 10(a)-(c)). In all assumed structures, the position of the first peak which recognizes the absorption edge is corresponding to their value of direct band gap at Γ point.

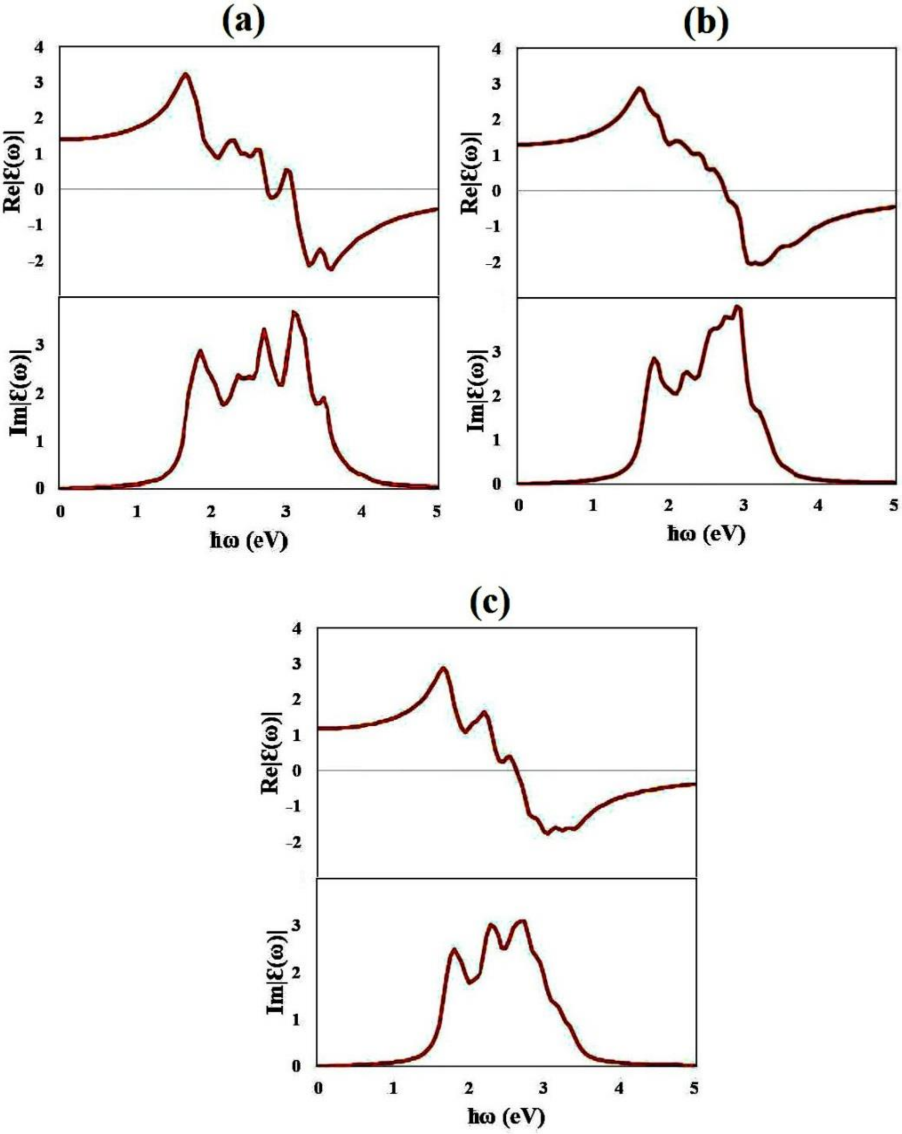

Fig.9 The imaginary and real parts of the dielectric function for (a) 9 A-SnCNR, (b) 10 A-SnCNR, and (c) 11 A-SnCNR

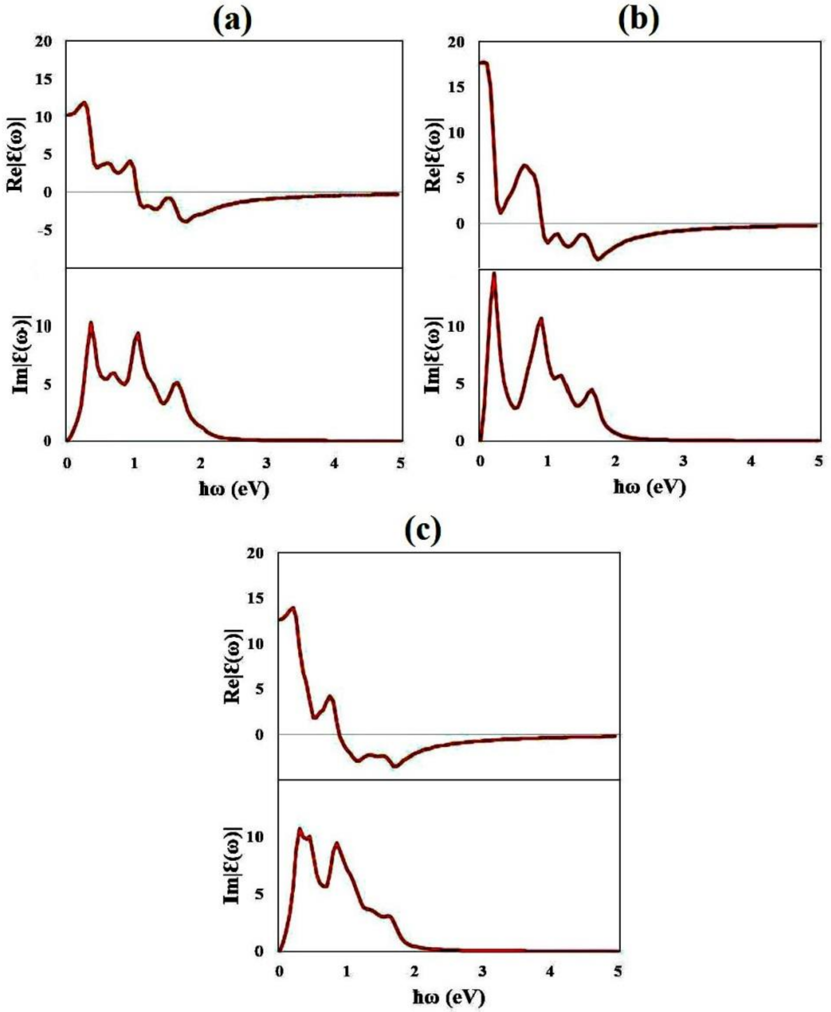

Fig.10 The imaginary and real parts of the dielectric function for (a) 9 A-SnGeNR, (b) 10 A-SnGeNR, and (c) 11A-SnGeNR.

The lower panel of figures 9 and 10 shows the real part of the dielectric function for A-SnXNRs. From the real part of the dielectric function, we obtain the static dielectric constant value ($\varepsilon_1(0)$). The dielectric constant values for 9, 11, and 13 A-SnXNRs are presented in Table 2.

TABLE 2
Dielectric constant values ($\varepsilon_1(0)$) and bandgap of W A-SnXNRs with width of W=9, 11, and 13.

Structure	**W A-SnCNRs**			**W A-SnGeNRs**		
Width (W)	9	11	13	9	11	13
Band gap energy (eV)	1.7	1.58	1.99	0.31	0.14	0.26
dielectric constant values ($\varepsilon_1(0)$)	2.39	2.03	2.18	11.19	11.18	13.63

In figure 11(a)-(f), we have shown the absorption coefficient which can be obtained from $\varepsilon_1(\omega)$ and $\varepsilon_2(\omega)$. In the case of 9, 11, and 13 A-SnCNRs, there is no absorption at the lower energy range from 0 to 1.2 eV (Infrared area) and the absorption spectrum appears at the partially infrared to Mid ultra-violet area. However, strong absorption characteristics for 9, 11, and 13 A-SnGeNRs appeared at near-infrared to the visible spectrum.

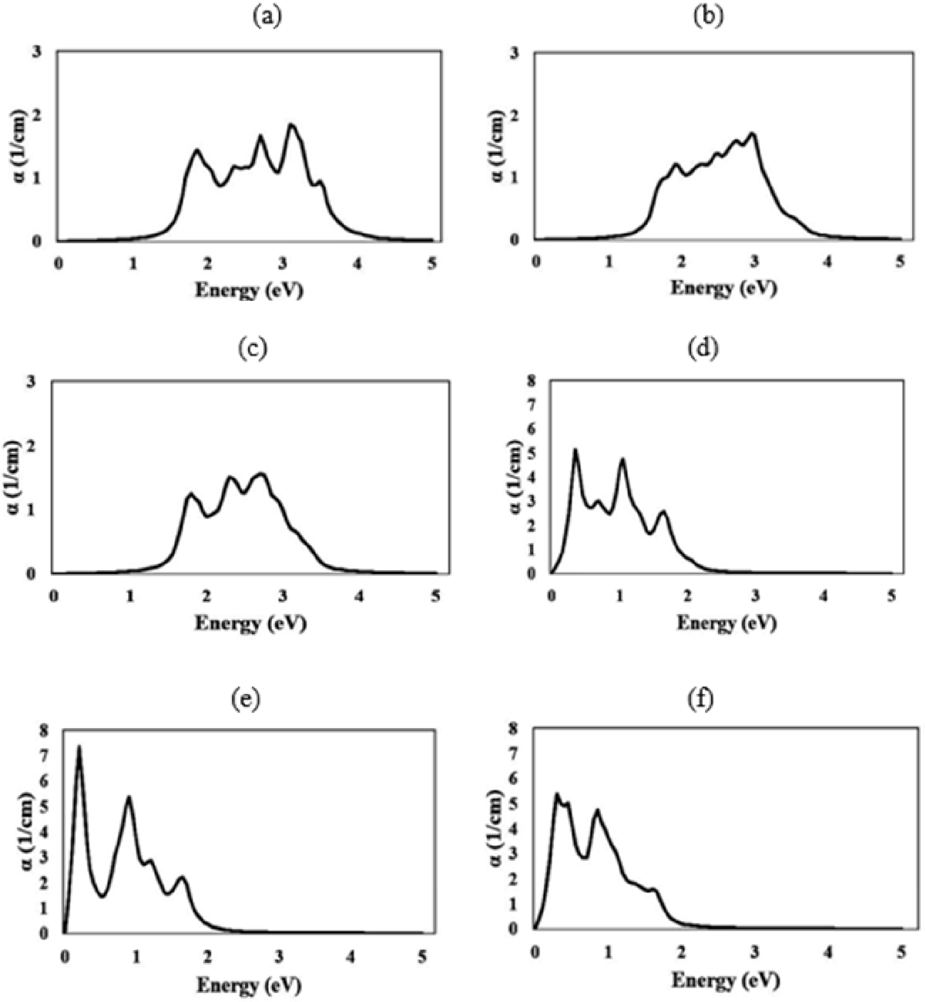

Fig.11 Absorption coefficient for (a) 9 A-SnCNR, (b) 11 A-SnCNR, (c) 13 A-SnCNR, (d) 9 A- SnGeNR, (e) 11 A-SnGeNR, and (f) 13 A-SnGeNR.

These observations open new opportunities for the SnXNRs in nano electronics and photonics applications.

4. CONCLUSION

Using a first-principles DFT method the electronic and optical properties of the planar SnCNRs and puckered SnGeNRs have been investigated. The band structures and DOS for A-SnXNRs with different widths (W=5 to 21) demonstrate that these materials behave as a direct bandgap semiconductor. It represents that tuning of band gap can be achieved by controlling the width of nanoribbons. Moreover, the Z-SnGeNRs are metal while Z-SnCNRs have very small band gap energy. Calculation of the optical properties of A-SnXNRs shows that their imaginary part of the dielectric function contains peaks that indicating the interband transition between the valence bands and the conduction bands. Therefore, these materials can be useful for optoelectronics applications. Also, the absorption coefficients for A-SnXNRs have been computed. These results provide a better understanding of one-dimensional nanostructures and their application in electronics devices.

REFERENCES

[1] Pourtajabadi, R., Nayeri, M. (2019). *'A Novel Design of a Multi-layer 2:4 Decoder using Quantum- Dot Cellular Automata*', Journal of Optoelectronical Nanostructures, 4(1), pp. 39-50

[2] Nayeri, M., keshavarzian, P., Nayeri, M. (2018). *'A Novel Design of Penternary Inverter Gate Based on Carbon Nano Tube'*, Journal of Optoelectronical Nanostructures, 3(1), pp. 15-26.

[3 Pourtajabadi, R., Nayeri, M. (2019). *'A Novel Design of a Multi-layer 2:4 Decoder using Quantum- Dot Cellular Automata*', Journal of Optoelectronical Nanostructures, 4(1), pp. 39-50.

[4] Hojatifar, M., Sahebsara, P. (2016). *'Tight- binding study of electronic band structure of anisotropic honeycomb lattice'*, Journal of Optoelectronical Nanostructures, 1(3), pp. 17-26.

[5] Mousavi, S. (2017). *'First–Principle Calculation of the Electronic and Optical Properties of Nanolayered ZnO Polymorphs by PBE and mBJ Density Functionals*', Journal of Optoelectronical Nanostructures, 2(4), pp. 1-18.

[6] Geim, A.K. and Novoselov, K.S., 2010. *The rise of graphene. In Nanoscience and Technology*. A Collection of Reviews from Nature Journals, pp. 11-19.

[7] Xie, C., Wang, Y., Zhang, Z.X., Wang, D. and Luo, L.B., 2018. *Graphene/semiconductor hybrid heterostructures for optoelectronic device applications.* Nano Today, 19, pp.41-83.

[8] Legesse, M., Rashkeev, S.N., Al-Dirini, F. and Alharbi, F.H., 2020. *Tunable high work function contacts: Doped graphene*. Applied Surface Science, 509, p.144893.

[9] Jayanetti, J.K.D.S. and Heald, S.M., 2006. *Preparation of SnGe Alloy Coated ge Nanoparticles and SnSi Alloy Coated si Nanoparticles by Ball-Milling. In*

Solid State Ionics. Advanced Materials for Emerging Technologies (pp. 870-877).

[10] Lin, S.S., 2012. *Light-emitting two-dimensional ultrathin silicon carbide*. The Journal of Physical Chemistry C, 116(6), pp.3951-3955.

[11] Enayati, M.H. and Mohamed, F.A., 2014. *Application of mechanical alloying/milling for synthesis of nanocrystalline and amorphous materials*. International Materials Reviews, 59(7), pp.394-416.

[12] Damizadeh, S., Nayeri, M., Fotooh, F.K. and Fotoohi, S., 2019. *First principles study of electronic structure and optical properties of armchair SnSi nanoribbons*. Materials Research Express, 6(9), p.095001.

[13] Xu, Z., Li, Y. and Liu, Z., 2016. *Controlling electronic and optical properties of layered SiC and GeC sheets by strain engineering*. Materials & Design, 108, pp.333-342.

[14] Majidi, S., Elahi, S.M., Esmailian, A. and Kanjouri, F., 2017. *First principle study of electronic and optical properties of planar GeC, SnC and SiC nanosheets*. Protection of Metals and Physical Chemistry of Surfaces, 53(5), pp.773-779.

[15] Fadaie, M., Shahtahmassebi, N., Roknabad, M.R. and Gulseren, O., 2017. *Investigation of new two-dimensional materials derived from stanene*. Computational Materials Science, 137, pp.208-214.

[16] Ding, Y. and Wang, Y., 2017. *Lattice thermal conductivities and thermoelectric performances of binary tin-based sheets: A computational study*. Applied Surface Science, 396, pp.1164-1169.

[17] Drissi, L.B., Ramadan, F.Z. and Kanga, N.B.J., 2018. *Optoelectronic properties in 2D GeC and SiC hybrids: DFT and many body effect calculations*. Materials Research Express, 5(1), p.015061.

[18] Luo, M., Yu, B. and Xu, Y.E., 2019. *Tuning Electronic Properties of the SiC-GeC Bilayer by External Electric Field: A First-Principles Study*. Micromachines, 10(5), p.309.

[19] Şahin, H., Cahangirov, S., Topsakal, M., Bekaroglu, E., Akturk, E., Senger, R.T. and Ciraci, S., 2009. *Monolayer honeycomb structures of group-IV elements and III-V binary compounds: First-principles calculations*. Physical Review B, 80(15), p.155453.

[20] Lü, T.Y., Liao, X.X., Wang, H.Q. and Zheng, J.C., 2012. *Tuning the indirect–direct band gap transition of SiC, GeC and SnC monolayer in a graphene-like honeycomb structure by strain engineering: a quasiparticle GW study*. Journal of Materials Chemistry, 22(19), pp.10062-10068.

[21] Majidi, S., Achour, A., Rai, D.P., Nayebi, P., Solaymani, S., Nezafat, N.B. and Elahi, S.M., 2017. *Effect of point defects on the electronic density states of SnC nanosheets: First-principles calculations*. Results in physics, 7, pp.3209-3215.

[22] Jin, H., Dai, Y. and Huang, B.B., 2016. *Design of advanced photocatalysis system by adatom decoration in 2D nanosheets of group-IV and III–V binary compounds.* Scientific reports, 6, p.23104.

[23] Peng, X., Copple, A. and Wei, Q., 2014. *Edge effects on the electronic properties of phosphorene nanoribbons.* Journal of Applied Physics, 116(14), p.144301.

[24] Kresse, G., and Furthmuller, J., Vienna ab-initio simulation package (VASP): The guide. VASP Group, Institut fur Materialphysik, Universitat Wien, Sensengasse, 2002, 8.

[25] Engel, E., Höck, A. and Varga, S., 2001. Relativistic extension of the Troullier-Martins scheme: Accurate pseudopotentials for transition-metal elements. Physical Review B, 63(12), p.125121.

[26] Perdew, J.P., Burke, K. and Ernzerhof, M., 1996. *Generalized gradient approximation made simple*. Physical review letters, 77(18), p.3865.

[27] Notash, S. and Fotoohi, S., 2019. *Spin polarized electronic and optical properties of vacancy defects in armchair phosphorene nanoribbons*. Materials Research Express, 6(11), p.116312.